Chapter 12
Group III–V and II–VI Quantum Dots and Nanoparticles

Alexander A. Guda, Mikhail A. Soldatov and Alexander V. Soldatov

By decreasing the size of semiconducting material the novel properties appear from the increased surface/bulk ratio and quantum confinement effects. X-ray absorption spectroscopy (XAS) can be applied to quantum dots and nanoparticles in-situ in the colloid, on the substrate or inside a solid matrix. The structural information about average size, phase composition, and growth orientation can be extracted from XAS along with information about electronic and magnetic properties of pure and doped nanostructures. In the chapter we shall describe the general properties of quantum dots and their applications that will help to understand the tasks for spectroscopy. Case studies will provide the information that is obtained from XAS complementary to other methods.

12.1 Properties and Applications of Quantum Dots

Nanoparticle (NP) and quantum dot (QD) are regarded as zero-dimensional nanostructures. The term "QD" is usually used for semiconductor nanoparticles and islands where quantum confinement of electrons and excitons determines their properties. Decades passed after the dependence of the spectral position of the exciton absorption lines of the nanosized CuCl crystals was attributed to the quantum size effect [1] and three-dimensionally confined semiconductor quantum wells or zero-dimensional semiconductor nanostructures showing discrete electronic states were named "QDs"

A.A. Guda (✉) · M.A. Soldatov · A.V. Soldatov
Southern Federal University, Sorge str. 5, Rostov-on-Don 344090, Russia
e-mail: guda@sfedu.ru

M.A. Soldatov
e-mail: mikhailsoldatov@sfedu.ru

A.V. Soldatov
e-mail: soldatov@sfedu.ru

C.S. Schnohr and M.C. Ridgway (eds.), *X-Ray Absorption Spectroscopy of Semiconductors*, Springer Series in Optical Sciences 190,
DOI 10.1007/978-3-662-44362-0_12

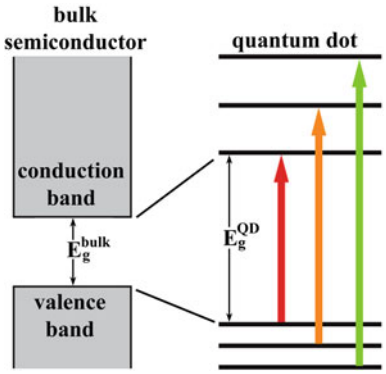

Fig. 12.1 The changes in the density of electronic states are shown schematically for different sizes of semiconductors

[2]. However it is still a hot topic due to the recored-breaking pace of developments in nanotechnology.

A QD can be thought of as an artificial atom, as its electron density of states consists of a series of very sharp peaks, and its physical properties resemble, in many respects, those of an atom in a cage. The discrete structure of energy states shown in Fig. 12.1 leads to a discrete absorption spectrum of QDs, which is in contrast to the continuous absorption spectrum of a bulk semiconductor. However these artificial atoms are also expected to have some significantly different properties compared with real atoms, as they can be filled with both electrons and holes [3].

The charge carriers inside QDs are confined in all three dimensions by the surface and thus the size and shape of QDs determine the energy spectrum of electronic levels [4]. It is possible to estimate the change of the QDs band gap energy with size R by applying the simple model of spherical potential well:

$$E_g^{QD} \approx E_g + \frac{\pi^2 \hbar^2}{2 m_{eh} R^2} \tag{12.1}$$

$$m_{eh} = \frac{m_e m_h}{m_e + m_h}$$

where m_e and m_h are the effective electron and hole masses correspondingly. The ability to precisely control the size of a QD enables the manufacturer to determine the desired emission wavelength.

The main advantages of QD include high quantum yields, broad absorption spectra, size-tunable emission spectra, and good resistance to chemical and photochemical degradation. QDs have the large surface which is highly reactive. Thus in colloids they are stabilized with surface reactants. Usually the appropriate shell covers the core of the QD in order to improve the photo-luminescence yield and prevent from degradation. Unterminated dangling bonds on the QD's surface can affect the emission efficiency because they lead to a loss mechanism wherein electrons are rapidly trapped at the surface before they have a chance to emit a photon.

Cadmium selenide has been used intensively as a cellular marker because CdSe emits in the visible domain and is an excellent contrast agent. ZnS layer can be used as a shell to protect the core from oxidation and also the leeching of CdSe into the surrounding solution. QDs are more resistant to degradation than other optical imaging probes such as organic dyes. Figure 12.2 shows pseudocoloured images depicting five-colour QD staining of fixed human epithelial cells. Each color was used for labeling the nucleus, Ki-67 protein, mitochondria, microtubules and actin filaments correspondingly. Right panel shows confocal fluorescence images of fixed HepG2 cells stained with glutathione-capped CdTe QDs. Nucleoli and cytoplasm were stained by QDs emitting green and red light correspondingly.

The possibility to tune the energy gap between electronic levels by changing the size of QD explains the great interest to such objects from nanoelectronics, quantum computing, light emitters and makes them desirable for solar cell use [7, 8].

Schematic explanation of the operation principle of the electron spin memory device based on Ga(In)As QDs is shown Fig. 12.3 [9]. Resonant excitation produces excitons in the QD. Axial electric field provided by the applied bias V_{store} ionizes

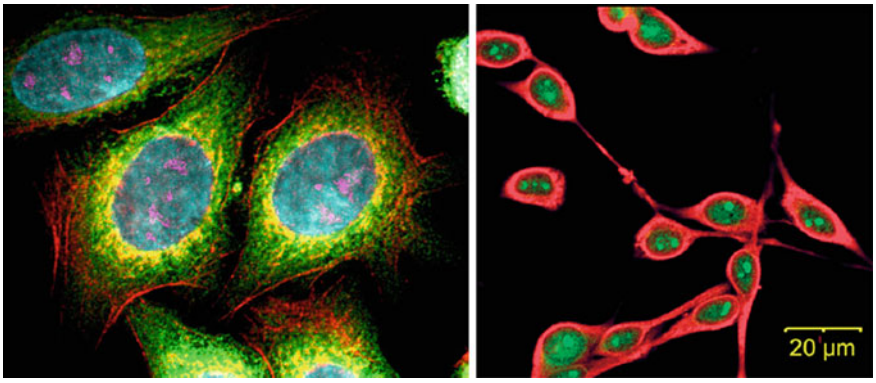

Fig. 12.2 Fluorescence images of epithelial cells (*left*, courtesy of Quantum Dot Corp) and HepG2 cells (*right*) stained with QDs QDs of specified size. Adapted from [5, 6]

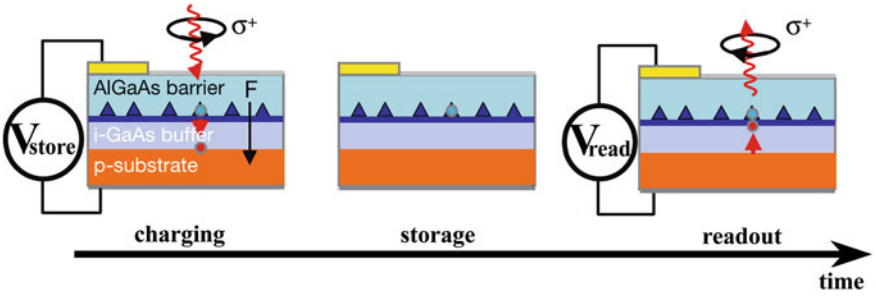

Fig. 12.3 Optically programmable electron spin memory using Ga(In)As QDs. Adapted from [9]

excitons. The AlGaAs barrier above the QD layer inhibits electron escape from the QDs and after charge separation, they are stored directly in the QDs. Readout is provided by applying the forward biasing to the device. When holes drift back into the QDs, they neutralize the stored charge. The polarization of generated photon probes the electron spin orientation.

12.2 Synthesis

First QDs were CuCl nanocrystals grown during high-temperature heating in the SiO_2 matrix [1]. Self-assembled QDs could be fabricated during the epitaxial growth, e.g. molecular beam epitaxy. QDs in material systems InAs/GaAs and InAs/InP are formed in Stranski–Krastanow regime as shown in Fig. 12.4. This means that InAs, is depositing layer-by-layer on the substrate with significantly mismatched lattice parameter [10]. Due to the large strains in the structure part of this material forms array of islands with diamond-like shape after the thickness of planar layer of InAs exceeds the critical value (in case of InAs on top of GaAs it is 1, 7 monolayer).

Using the chemical beam epitaxy the QDs can be realized as layers inside nanowires as shown in Fig. 12.5. Longitudinal quantization exceeding 10 meV has been observed in transport measurements on 50–70 nm diameter InAs nanowires with two InP barriers [11]. Changing the dot size L allows designing QDs along a nanowire with different specific spin splittings in a constant magnetic field. In future this is expected to allow individual gate tunable spin splittings in a series of dots along a nanowire which makes nanowire QDs containing a single electron spin interesting

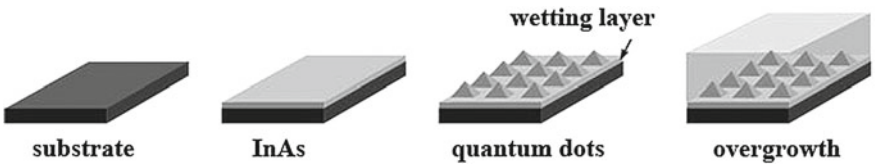

Fig. 12.4 Stranski-Krastanow regime of InAs/GaAs formation process

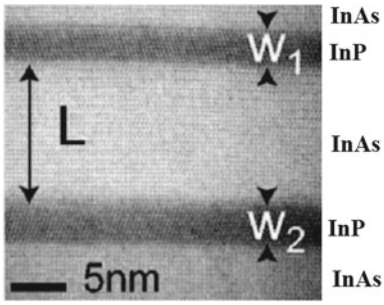

Fig. 12.5 High-resolution STEM image of a QD inside a nanowire. L = 12 nm is defined as the length of the In As segment between two InP barriers with widths W1 and W2. Figure adapted from [11]

systems for the realization of cubits. Authors in [12] have shown the possibility to produce QDs inside a homogeneous nanowire. By changing the InP crystal structure from zinc-blende to wurtzite a system similar to one in Fig. 12.5 was formed.

A metal-organic chemical vapor deposition technique was used to for controllable growth of ZnO/MgO quasi core-shell QDs [13]. Silicon ⟨111⟩ wafers were used as the substrates. Diethylzinc (DEZn), bis(methylcyclopentadienyl) magnesium ($(MeCp)_2Mg$), and O_2 were used as the zinc source, magnesium source, and oxygen source, respectively. N_2 was used as the carrier gas. The growth temperature was 400 °C. The chamber pressure was maintained at 3 and 6 Pa during the growth of ZnO and MgO, respectively. An exciton emission from ZnO QDs was greatly enhanced after the growth of MgO layer. TEM image of ZnO/MgO core shell QD is shown in Fig. 12.6.

The easiest way to produce macroscopic quantities of QDs is the hydrothermal synthesis. A unified approach through liquid–solid–solution (LSS) process can be used to synthesize a broad range of nanocrystals—from noble metals to the semiconductors [14]. Figure 12.7 shows cadmium selenide QDs and their size distribution after hydrothermal synthesis.

The QDs in colloid solution are covered by the layer of organic molecules which prevents uncontrolled growth and agglomeration of the nanoparticles. When coated with a suitable, chemically active surface layer, QDs can be coupled to each other or to different inorganic or organic entities and thus serve as useful optical tags.

XAS can probe the chemical bonding between surface atoms and surfactants. The ligand for the biological applications should possess a strong affinity for the QD surface. Ligand exchange is the method used to replace the original hydrophobic surface ligands on the QD surface with hydrophilic ligands or to attach to the QD a cell-penetrating peptide in order to allow QDs penetration into the living cells [15, 16]. Thiol groups as in Fig. 12.8 have been the most frequently utilized as anchors on the QD surface since they have strong affinity with Cd and Zn. In order to avoid surface reactants the in-water laser ablation can be used [17].

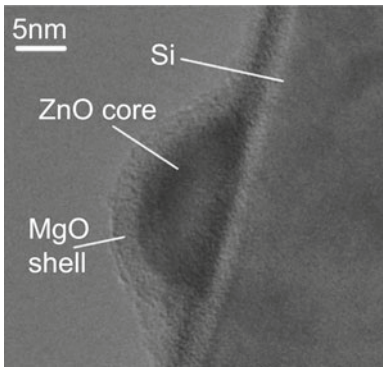

Fig. 12.6 Cross-sectional TEM image of a selected ZnO/MgO core-shell QD. Adapted from [13]

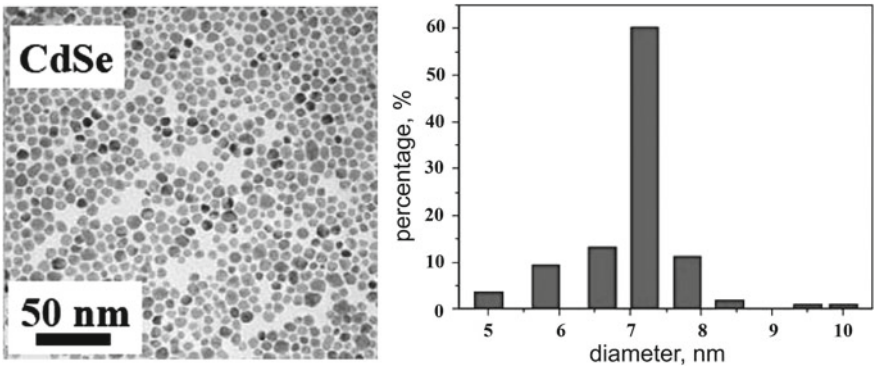

Fig. 12.7 CdSe nanocrystals and their size distribution. 300 particles were measured to get the size distribution. Adapted from supplementary data of [14]

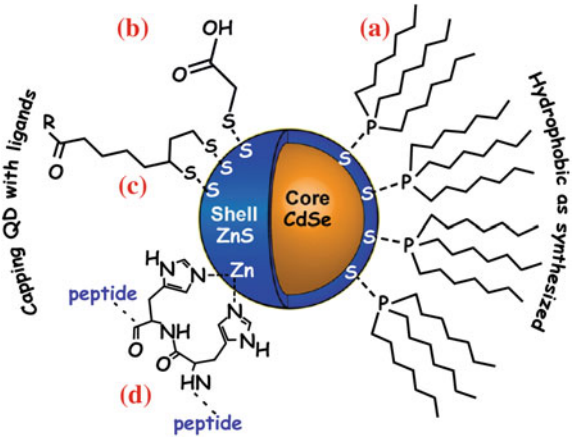

Fig. 12.8 Ligands attached to the QD in colloid. **a** trioctylphosphine (TOP/TOPO) **b** monodentate thiol; **c** bidentate thiol; **d** histidine-appended peptides. Adapted from [15]

Nanoparticles can be effectively produced by means of high-energy ball milling. For example ZnS QDs with cubic phase have been prepared by mechanical alloying the stoichiometric mixture of Zn and S powders at room temperature in a planetary ball mill under Ar [18].

12.3 Methods to Study the QDs

The size distribution of QDs can be studied by direct methods such as electron microscopy or atom probe microscopy. These methods allow studying the crystal planes with atomic resolution as well as single dopants in semiconductors [19]. Indirect methods including X-ray diffraction, small-angle X-ray scattering, optical scattering, optical absorption and emission can be used as well.

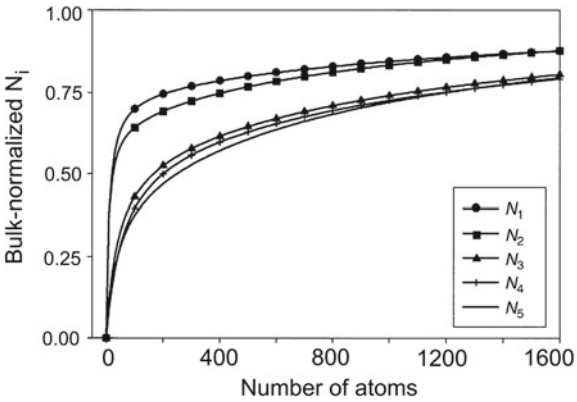

Fig. 12.9 Correlation between N_i coordination number normalized to the bulk value and total number atoms in the nanoparticle. Adapted from [20]

The X-ray absorption fine structure (XAFS) can be used to analyze the oxidation state, crystal structure and size of QDs. This method is favorable for the local defects inside QDs and when QDs of a small size are analyzed. The extended X-ray absorption fine structure (EXAFS) contains information about coordination numbers of absorbing atoms i.e. one can determine the first, second, third etc. coordination numbers for a given sort of atoms in QD. Figure 12.9 shows how first, second, third etc. coordination numbers depend on the total number of atoms in QD [20]. These curves represent a fit over wide range of densely packed nanoclusters with different shape.

Coordination numbers decrease when the cluster size decreases and thus the values obtained from EXAFS-analysis can be used to estimate the cluster size. Functions for the first N_1 and second N_2 coordination shell approach much faster the values from bulk compared with the higher coordination shells. Consequently, the accuracy of the clusters size determination strongly depends on the number of atoms as well as on the order of the coordination shell analyzed.

The near-edge X-ray absorption fine structure (NEXAFS) is a useful detection method for crystal structure modifications in nano-scale systems. Gilbert et al. [21] found that low energy L-edge absorption is sensitive to the structural transition from wurtzite into zinc blende for ZnS due to high energy resolution obtained in the experiment. Figure 12.10 shows the corresponding experimental spectra above S L-edge and Zn L-edge.

One can use different X-ray polarizations to study the crystal phases as well as the growth direction of nanostructures. For the wurtzite structure with a preferential direction, *c-axis,* one can observe X-ray linear dichroism (XLD) in contrast to the case of zinc blende where X-ray absorption is isotropic [22]. In case of wurtzite nanostructures the XLD signal will be present for the oriented nanowires while nanoparticles and QDs shall not exhibit dichroism, as shown in Fig. 12.11.

The Zn K-edge was less sensitive to the W-ZB phase transformation. However in case of high pressure transition into the NaCl phase the Zn K-edge X-ray absorption

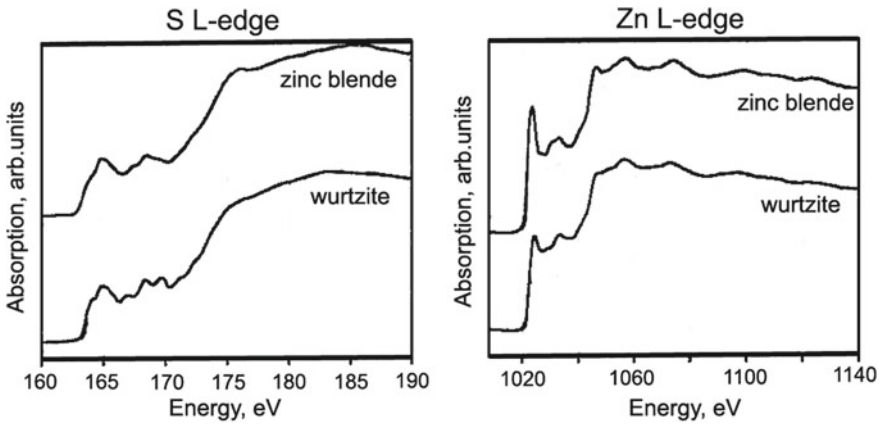

Fig. 12.10 Experimental NEXAFS of ZnS zinc blende and wurtzite polytypes. Adapted from [21]

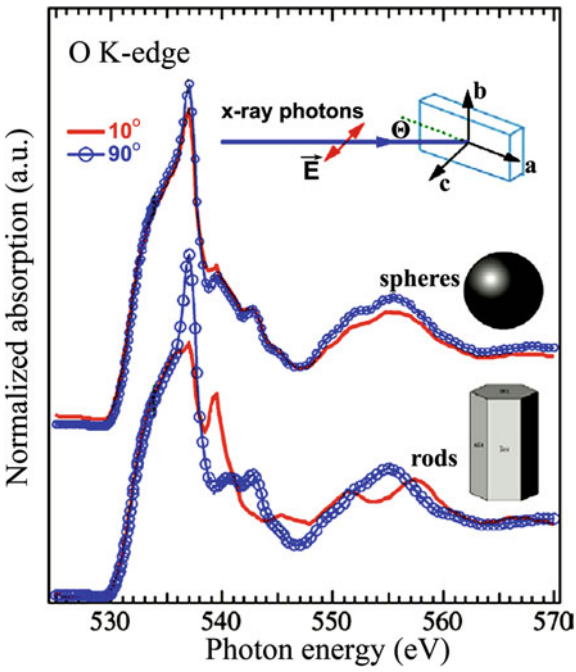

Fig. 12.11 Polarization-dependent X-ray absorption spectra of zincite ZnO isotropic spherical nanoparticles and anisotropic rod-like morphology. Adapted from [23]

near-edge structure (XANES) spectra reveal striking differences [24]. Figure 12.12 shows how Zn K-edge fine structure changes for the ZnO under different pressure.

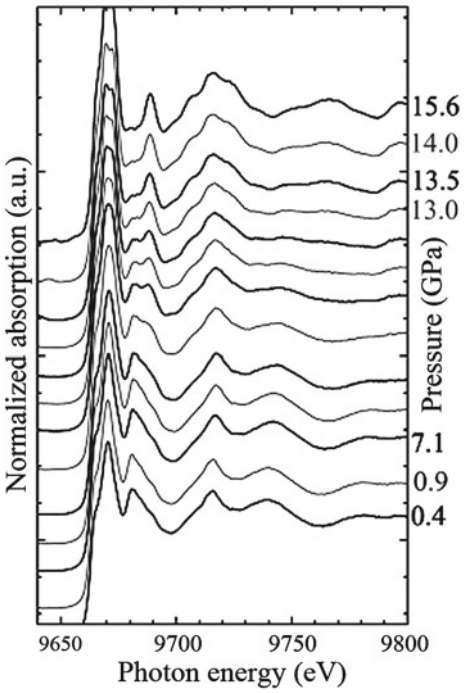

Fig. 12.12 Zn K-edge XANES spectrum of bulk ZnO as a function of applied pressure. Adapted from [24]

12.4 Case Studies

The determination of the magnitudes of elastic deformations in thin layers and nanocrystals by conventional methods of X-ray diffraction analysis or electron diffraction techniques is limited by their sensitivity and by the absence of long-range order in such systems. EXAFS and XANES spectroscopy methods, in which powerful continuous-spectrum X-ray sources are used, provide a unique opportunity to solve such problems. Using powerful synchrotron radiation, EXAFS and XANES spectroscopies allow one to determine the local environment characteristics of atoms (interatomic distances, coordination numbers, environment symmetry, types of neighboring atoms, and Debye-Waller factors). Electron level shifts and charge state of atoms can be analyzed as well..

12.4.1 Group III–V QDs and Nanoparticles

Variations in the microscopic structural parameters of Ge/Si, GaN/AlN, and InAs/AlAs QDs such as interatomic distances, coordination numbers, and types of neighboring atoms are determined by the EXAFS and XANES spectroscopy methods

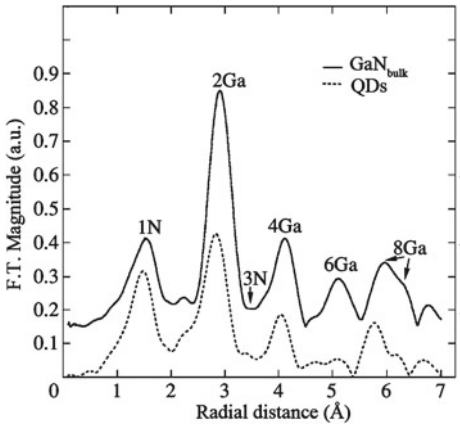

Fig. 12.13 The magnitude of FT for the bulk GaN and the GaN/AlN QDs at the Ga K-edge. Adapted from [25]

[25]. A detailed description is given to GaN/AlN Ga K-edge EXAFS (Figs. 12.13 and 12.14 and 12.15) and InAs/AlAs heterosystems (Fig. 12.16).

The authors fit Fourier-filtered data with k- and k^2 -weighting in the range of photoelectron wave vectors from 3 to 14 $Å^{-1}$. The Fourier-filtered experimental data in the ranges 1.0 Å < R < 1.8 Å and 2.5 Å < R < 3.3 Å for the first (N) and the second (Ga) coordination spheres of Ga, respectively, were used to perform the fitting procedure.

It is found that the Ga-N interatomic distance in the heterostructure with GaN QDs decreases by ∼0.02 Å in comparison with bulk GaN and is equal to ∼1.93 Å. The Ga–Ga interatomic distance in the heterostructure with GaN QDs decreases by ∼0.05 Å in comparison with pure GaN and is equal to ∼3.13 Å. Further XAS studies of GaN are presented in Chaps. 3 and 13.

Eu-doped GaN QDs embedded in AlN matrix have been studied by means of EXAFS technique [26]. Each QD sample consisted of 10 stacked planes of GaN QDs separated from one another by a 12 nm-thick AlN spacer. Due to the large difference in band gap energy between AlN and GaN, strong confinement of carriers in GaN QDs is expected, which leads to a remarkable persistence of photoluminescence up to room temperature.

To investigate Eu incorporation Eu L_3 EXAFS experiments were performed at the FAME beamline (BM30B) at the European Synchrotron Radiation Facility in Grenoble. Spectra were recorded in fluorescence mode and samples were cooled with liquid nitrogen. All recorded spectra clearly show two contributions in the L_3 edge, corresponding to the Eu^{2+} edge and the Eu^{3+} edge. Eu^{2+} can be attributed to the europium oxide monolayer that typically accumulates on the surface. Thus EXAFS oscillations were extracted relative to the Eu^{3+} edge.

EXAFS results obtained for a sample with 2.7 % Eu-doped QDs are presented in Fig. 12.14. It is important to determine whether Eu has been substitutionally incorporated inside GaN or undesirable AlN doping occurred. The first coordination shell of Eu both in AlN and GaN consists of nitrogen and thus one has to assess the chemical

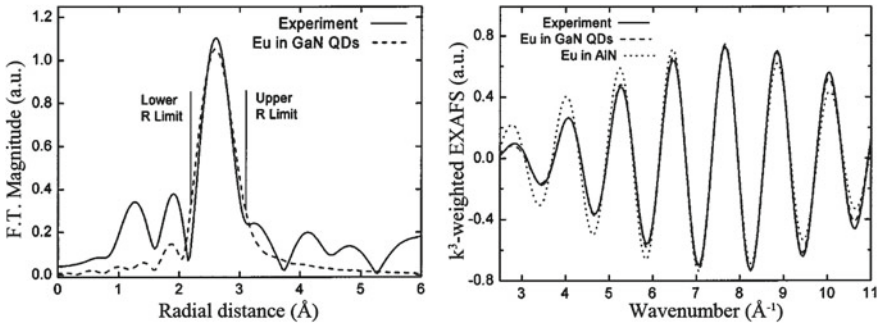

Fig. 12.14 Experimental and calculated Eu L_3-edge EXAFS in R- and q-space for Eu doped GaN QDs embedded in AlN matrix. *Dashed line* correspond to the simulation for Eu in GaN. *Dotted line* is a simulation for Eu in AlN. Adapted from [26]

nature of the second nearest neighbor shell of Eu. Second shell consists of 12 Ga for Eu inside GaN QDs and 12 Al inside the AlN matrix. These backscatterers are easily distinguishable because of the large discrepancy in mass between Al and Ga. The pseudoradial distribution in R (left part in Fig. 12.14) was obtained by taking the norm of the Fourier transform of $k^3\chi(k)$, with k ranging from 2.6 to 11.1 $Å^{-1}$. Nitrogen and oxygen in the first coordination shell of Eu give rise to the small two peaks between 1.0 and 2.1 Å. Second shell gives rise to the peak at 2.6 Å. EXAFS analysis was conducted on this second peak by Fourier backtransform (right panel in Fig. 12.14) with R ranging from 2.2 to 3.1 Å. Backtransform spectra clearly indicate that Eu is embedded into GaN QDs while poor agreement with experiment is found for the model when Eu incorporates in AlN. Doping of GaN is also discussed in Chaps. 4 and 13.

It was shown that EXAFS in total reflection geometry (ReflEXAFS) can be effective in determining the structure of $In_xGa_{(1-x)}As$ QDs grown on GaAs [27]. ReflEXAFS data from thin surface systems are not contaminated by anomalous dispersion effects so they can be directly treated as conventional EXAFS spectra. In particular, authors claim that it is possible to recognize the strained or relaxed state of the dots as well as their composition by comparing theoretical models to experimental data on first shell bond lengths. The Fourier transforms with the superimposed best fitting curves are shown in Fig. 12.15 whereas the inset shows the raw EXAFS spectra. Well defined first shell coordination is evident at approximately 2.25 Å (value without phase correction). XAS studies of unstrained $In_xGa_{1-x}As$ are also discussed in detail in Chap 2.

Specific variation of XAFS method—capacitance XAFS was applied to study the local structure of an As atom in the self-organized InAs QD arrays inside GaAs matrix [28]. The X-ray-induced photoemission of confined electrons in a QD via inner-shell absorption was detected by a capacitor and the photon energy dependence of the capacitance provided the XAFS spectrum of the atom in the QD. It was found that when the bias voltage applied to the system aligned the Fermi energy with the

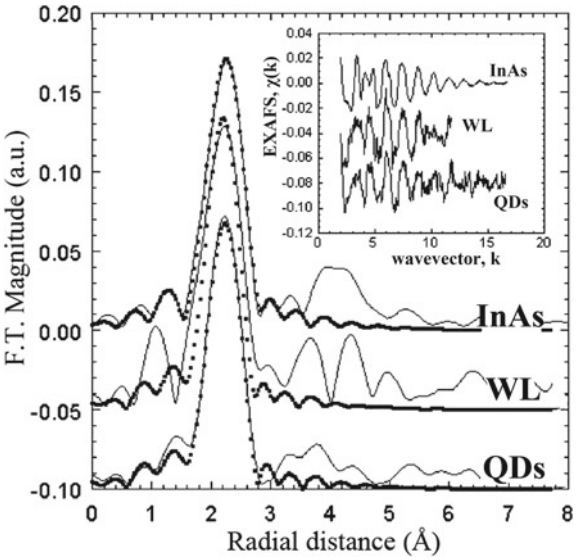

Fig. 12.15 Fourier transforms of the k^2-weighted EXAFS spectra calculated in the range $k = 3 \ldots 10$ Å^{-1}. Inset show χ(k) data. Continuous *lines* are the experimental data, the *dotted lines* are the best fits done in R space in the range R = 1.5 . . . 2.7 Å. InAs—*bulk*, WL-wetting layer, *Dots* -QDs. Adapted from [27]

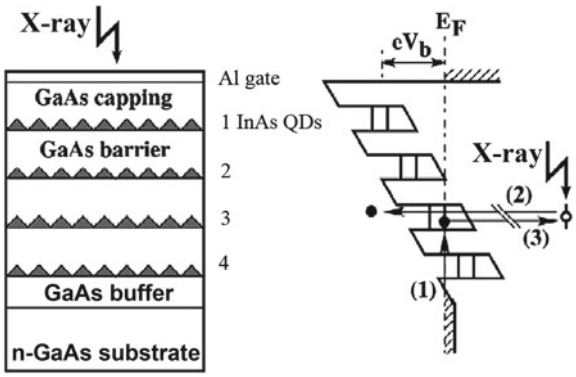

Fig. 12.16 Proposed concept for selective observation of QD by the capacitance XAFS method. *Left* typical sample structure. *Right* expected electron transition process in the sample. Adapted from [28]

quantum electronic level, the site-selectivity of XAFS could be enhanced. The peak energy shift of about 1.5 eV was observed in the site-selective XAFS spectrum of an As atom in the system of QD. Theoretical simulations indicated that this energy shift originated from the atoms in the point defect position at the boundary between an InAs QD and a GaAs barrier layer [28].

The interface effect of InSb QDs embedded in SiO_2 matrix was investigated by XAFS (both of EXAFS and XANES regions) [29]. The EXAFS showed in Fig. 12.17 suggested the bond length of the Sb-In first shell of the InSb QD to be contracted by about 0.02 Å compared with that of the bulk InSb. Theoretical analysis of the Sb K-XANES of InSb QDs embedded in SiO_2 matrix made it possible to conclude that the intensity increase and broadening of the white line peak were mainly due to the increase of Sb p-hole occupation and the change of Sb intra-atomic potential affected

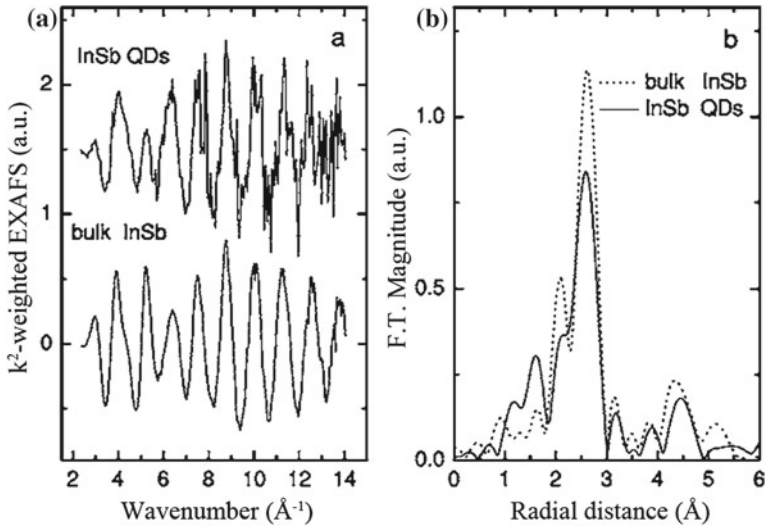

Fig. 12.17 **a** Sb K-edge EXAFS functions $k^2\chi(k)$ of the bulk InSb and the InSb QD. **b** Fourier transforms of the bulk InSb and the InSb QD. Adapted from [29]

by the SiO_2 matrix. Thus, the interaction between the InSb QDs and SiO_2 matrix resulted not only in slight lattice contraction of InSb QDs and structural distortion of the interface, but also leaded to the significant change of the Sb intra-atomic potential and the charge redistribution of Sb atoms.

12.4.2 Group II–VI QDs and Nanoparticles

Seehra et al. [30] reported size-dependent ferromagnetism in TOPO-capped (tri-n-octylphosphine oxide) CdSe QDs observed by means of combined XANES and EXAFS study. The article covers such points as measuring the number of unoccupied states or d-holes on the Cd site for 2.8, 4.1, and 5.6 nm CdSe QDs. It is shown that this ferromagnetism is due to d-holes on the Cd site bonded to TOPO created by experimentally observed charge transfer from Cd to TOPO.

The authors measured charge transfer from Cd to TOPO invoked in their interpretation of ferromagnetism using XANES spectra of TOPO-capped CdSe QDs. Figure 12.18a shows an increase in the Cd K-edge white line intensity with QDs size reduction indicating an increase in the number of unoccupied states above the Fermi level. An increasing charge loss in the occupied states of Cd ion with decreasing QDs size is also stated. The additional charge transfer to Se in CdSe QDs induced by capping with TOPO lead to decrease in the lattice constant with decreasing QDs size. Figure 12.18b shows Fourier transform (FT) of the EXAFS $k^2\chi$ data at the Cd K-edge. It is claimed that weaker intensity of the oscillation for the smaller sizes

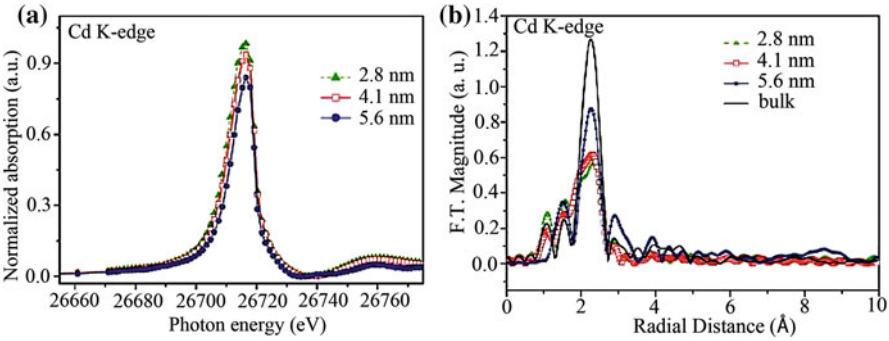

Fig. 12.18 **a** Normalized and background corrected Cd K-edge XANES spectra for CdSe QDs. **b** Fourier transforms amplitudes of the EXAFS $k^2\chi$ data at the Cd K-edge for 2.8, 4.1, 5.6 nm, and bulk CdSe. Adapted from [30]

indicates more disordered local structure. It is also pointed out that the decrease in the amplitude of the peak near 2.27 Å in the FTs due to Cd–Se bond length with decreasing size indicates reduction of the coordination number of Cd and increase of the local disorder. Also the additional feature that is shown on the low energy side is due to Cd–O bond for the smaller QDs. The paper claims that these observations strongly support the assumption of charge transfer between Cd and oxygen that would deplete the otherwise full $4d^{10}$ band of Cd, creating holes and producing a net magnetic moment for Cd atoms bonded to TOPO on the surface of the CdSe QDs.

EXAFS has been applied to investigate a local structure for the CdSe/ZnSe QDs grown by molecular beam epitaxy (MBE) and migration-enhanced epitaxy (MEE) [31]. The article covers such points as the intermixing of Cd and Zn atoms, chemical compositions and strain induced by cap-layer studied by means of EXAFS at the Cd K-edge. The paper claims that from the qualitative analysis the number of oscillations for QDs and the bulk CdSe is similar, however the second coordination shell between 3.5 and 4.5 Å depicted in Fig. 12.19 is broader for the QDs in comparison to the bulk one, suggesting the existence of more than one species' of atoms in this shell.

Structural parameters for investigated and reference CdSe result from the fitting analysis. It is reported that the first coordination shell in the QDs is composed by 4 Se near-neighbors, while the second one is composed by a mixture of Cd and Zn and the coordination number is kept 12 as follows from the nominal zinc-blende lattice. It is also reported that the Cd–Se bond length was determined as 2.61 Å and the next-neighbor distance Cd–Cd in the second coordination shell is larger by about 0.06 Å from that in the pure CdSe compound (4.31 Å), whereas the bond length Cd–Zn was found to be 4.18 Å. It is also stated that the value of the Debye–Waller factor for distances Cd–Se and Cd–Cd is similar to this found for reference CdSe compound.

The array of ZnO nanowires decorated by different-sized InP QDs were proposed for splitting water with a substantially enhanced photocurrent. The conduction band properties of ZnO nanowires with InP QDs was investigated by the Zn K-edge XAFS

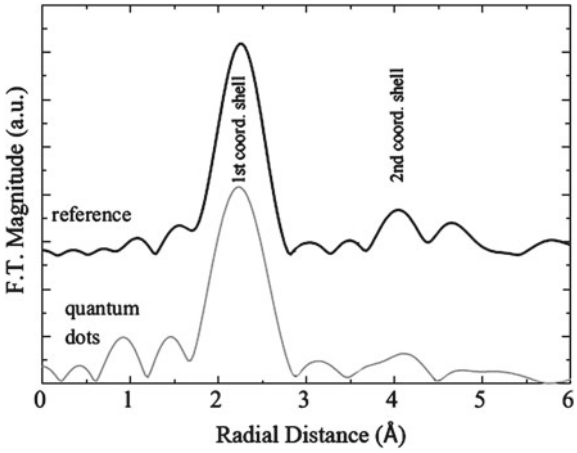

Fig. 12.19 The magnitude of FT for the bulk CdSe and the CdSe/ZnSe QDs at the Cd K-edge. Adapted from [31]

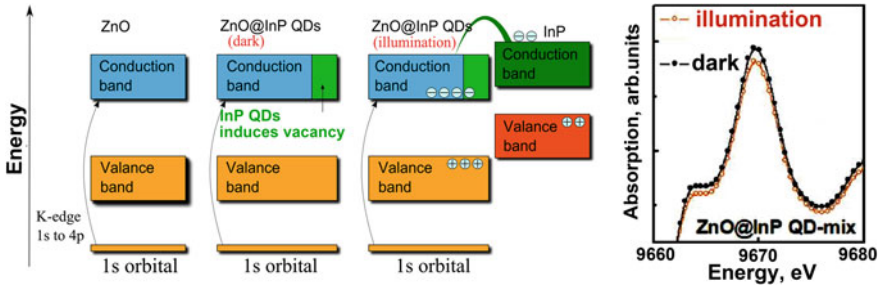

Fig. 12.20 Band structure evolution of the ZnO nanowires system covered with InP QD and changes in the Zn K-edge X-ray absorption spectrum under illumination. Adapted from [32]

analysis for both solar illuminated and not illuminated cases [32]. It was found that the orbital coupling occurred in the c axis direction of the ZnO nanowire. Because the white line intensity of XANES is proportional to the density of unoccupied states of the absorbing atoms these unoccupied states of the conduction band could enhance the transition probability from valence band to conduction band as shown in Fig. 12.20. Solar illumination of the system under the study made it possible to investigate the contribution from photoelectrochemical response. ZnO decorated with InP QDs had a significant increase in photogenerating electrons in the 4p orbital. One could attribute this increase of photogenerating electrons to the absorption of InP QDs in the visible region and the photogenerating electrons transfer from the conduction band of InP to that of ZnO. The contribution of photoresponse from ZnO nanowires or InP QDs could be distinguished by comparing the XAFS spectra collected under illuminated and not illuminated conditions. Further XAS studies of ZnO nanowires, both pure and doped, are reviewed in Chap. 13.

Cr-doped ZnSe QDs were studied by the Cr $L_{2,3}$-edge XAFS analysis [33]. Because it is well established that the Cr ion can be incorporated into ZnSe with variable oxidation states one should control the oxidation state of Cr ion inside the ZnSe QD. The energy positions of the spectral features and the shape of the Cr $L_{2,3}$-edge of the $x = 2.5\,\%$ $Zn_{1-x}Cr_x$ Se QD in Fig. 12.21 allowed an assignment of the Cr oxidation state as Cr^{3+} on the basis of a comparison to simulated $L_{2,3}$-edge XANES spectra from [34].

Chromium ion was found to be in the tetragonally distorted O_h site with a crystal field of $10\,Dq = 2.07\,eV$ due to pair formation of Cr octahedral by removal of three Zn ions for each pair of Cr ions in the lattice. The analysis of the data obtained made it possible to conclude that the sharing of the O_h edge by the Cr(III) ions in the ZnSe lattice produces a minimally distorted site in the lattice analogous to spinel inclusions in bulk metal chalcogenide structures [33]. XAS studies of Cr doped ZnTe are discussed in Chap. 16.

Microbeam X-ray absorption near edge structure (μ-XANES) technique was used for the analysis of the physicochemical changes of CdSe-ZnS core-shell QD in vivo [35]. A specific kind of worms—namely Caenorhabditis elegans have been studied to investigate the biological effects of QDs. Because in CdSe-ZnS core-shell QDs, selenium atoms are located in the core encapsulated by a ZnS shell, its chemical state changes only if the ZnS shell structure is degraded. Thus, the authors analyzed in situ Se K-edge μ-XANES spectra of QDs within the worms. The Se K-edge XANES of CdSe QDs mainly monitors the unoccupied p states of the Se element. It was found that at positions where XRF mapping matches well with optical fluorescence imaging, all the XANES spectra are similar to the original QDs with only slight differences as shown in Fig. 12.22. Interestingly, XANES of QDs after digestion where QDs fluorescence quenched showed obvious differences in intensity of some peaks and the energy position of the peaks (mostly a shift to higher energy by about 2 eV) and intensity of a shoulder gradually decreased. All these changes could be together assigned to a transition to oxidized Se like in Na_2SeO_3 compound. Thus, it was suggested that Se ion in the CdSe core is oxidized to SeO_3^{2-} after digestion in a worm. The changes of Se XANES spectra may be attributed to the collapse of core/sell structure after digestion, and the efficient protection of the CdSe core by ZnS shell is destroyed after 24 h of digestion in a worm.

XAFS spectroscopy at Cd L_3 edge and ab initio modeling of the experimental spectra were used to investigate the effects of surface passivation on the unoccupied electronic states of CdSe QDs covered with trioctylphosphine oxide (TOPO) or hexadecylamine (HDA) ligands [36]. Authors indicate that nitrile impurities present in the HDA bind to the surface of CdSe QDs during synthesis and lead to a mixing HDA and nitrile surfactant coating. Thus QDs synthesized in HDA are referred to as CdSeHDA/CN. It was found that there are considerable variations in the XAS spectral features as a function of size. The spectra for bulk CdSe and the 25 Å CdSe-HDA/CN QDs are closely comparable but increasingly pronounced changes in the absorbance are evident beyond the absorption edge as the QD radius decreases. The dependence of the XAS data on size provides a strong indication that these spectral variations are surface-related because the reduction in QD radius is accompanied by

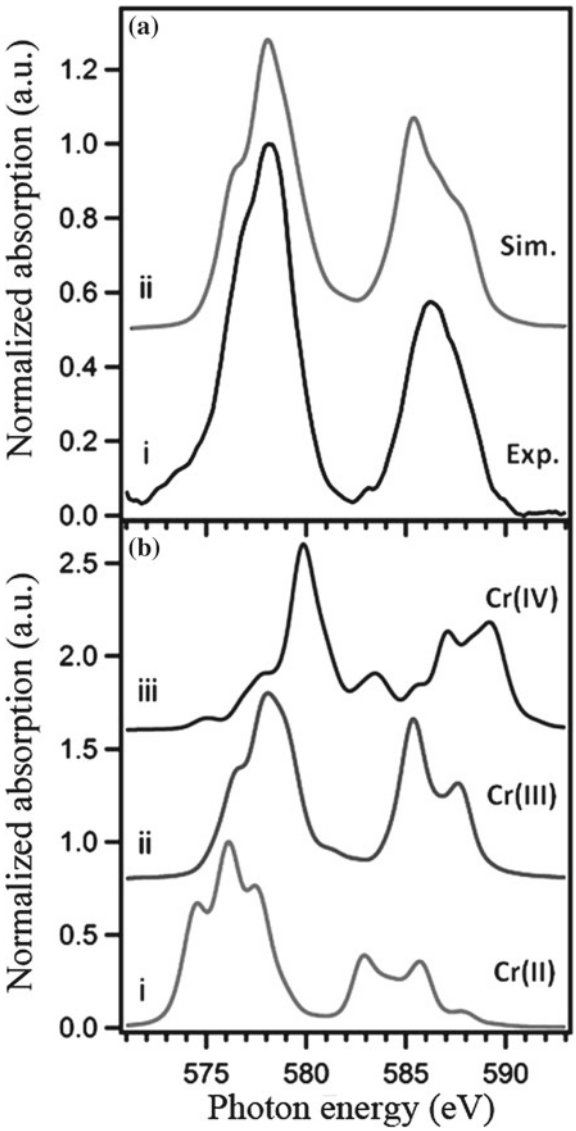

Fig. 12.21 Cr $L_{2,3}$-edge XAFS spectra [33]. **a** experiment on Cr-doped ZnSe QD and theory for tetragonally distorted O_h crystal field. **b** XAFS simulations of Cr ions in a perfect O_h field

a substantial increase in the fraction of surface Cd atoms and by a greater extension of the surface contribution to the overall signal. The conclusion was done that the surface ligands are primarily responsible for the differences in the shape of the XAS spectra.

The ligand exchange results in profound changes to the XAS data as shown in Fig. 12.23. XAS spectra demonstrate that the associated changes in unoccupied electronic structure arise due to interactions between the nitrile moieties and surface

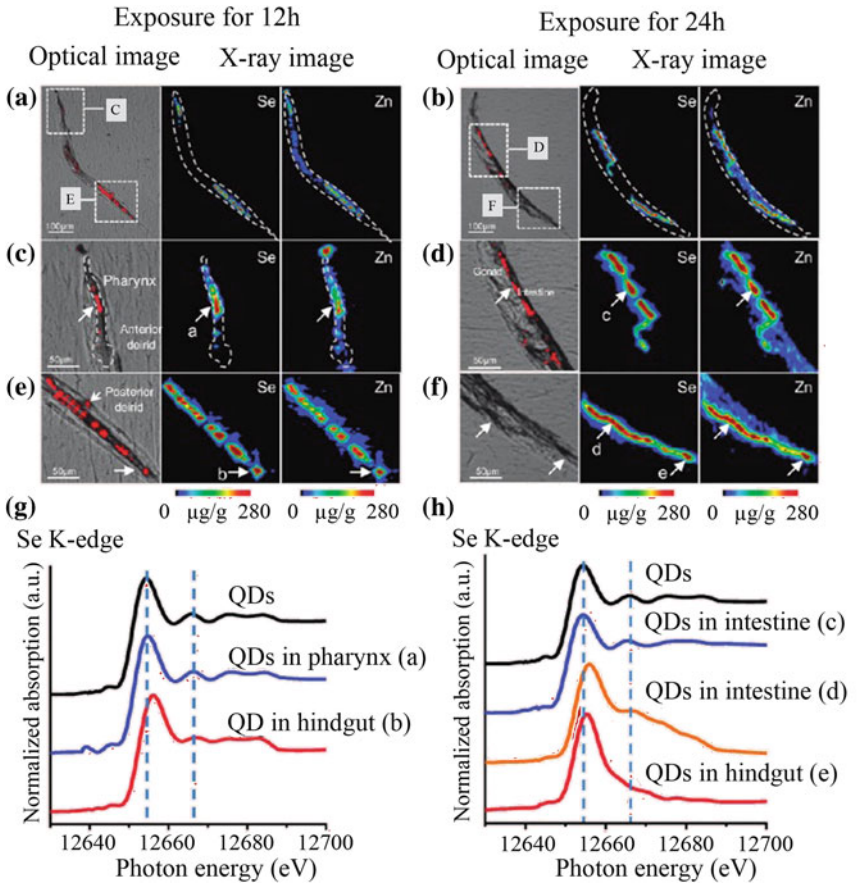

Fig. 12.22 Elemental analysis and QD degradation in a worm hermaphrodite *C. elegans*. (*A, B*)—optical fluorescence image (*gray*) versus X-ray fluorescence mapping of the whole worm exposed in CdSe-ZnS QDs for 12 and 24 h correspondingly. (*C–F*) similar images for the enlarged parts of the worm body shown by the *dashed lines* in *A* and *B*. (*G, I*) - in-situ Se K-edge µ-XANES at selected points *a–e* shown by *arrows*. X-ray spot size 5 × 5 µm. Adapted from [35]

Cd atoms. A particularly interesting feature of CdSe QDs is that the studied ligands primarily affect unoccupied electronic states several eV above the absorption edge rather than in the gap, as one might have predicted for surface states. This is consistent with the fact that the optical properties are not affected yet there is a ligand dependent change in the electronic structure, which could be responsible for the novel magnetic properties of the QDs [36].

Electronic structure and atomic arrangement of CdSe QD doped with Cu were studied by the Cu L_3 and Se L_3XAFS [37]. It was found that the L_3-edge stays at nearly a constant energy through the doping range of 2–15 molar percent. The observation of a constant L_3-edge energy (equal to the energy for CuI spectrum)

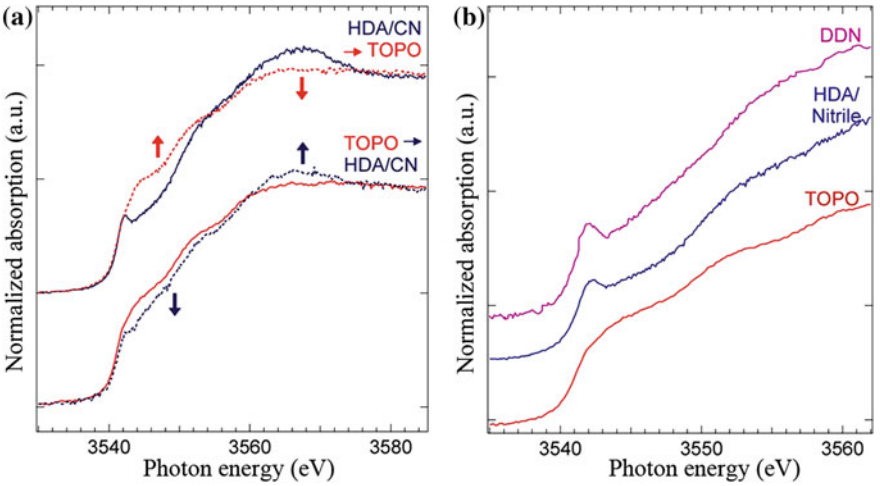

Fig. 12.23 The Cd L_3 -edge XANES **a** as prepared CdSe-HDA/CN QDs following ligand exchange with TOPO and as prepared CdSe-TOPO QDs following ligand exchange with 90 % HDA (including nitrile contaminants). **b** 15 Å CdSe-TOPO QDs following ligand exchange with DDN and reference 15 Å CdSe-TOPO and CdSe-HDA/CN QD spectra. Adapted from [36]

indicates that the oxidation state of the Cu ions in the CdSe QD is Cu(I) through all doping concentrations studied. This constant oxidation state is also an indication for the fact that Cu ion in the CdSe QD is a highly localized defect with very little charge transfer to the host lattice. The Se L_3 absorption edge shows the shifts to lower energy by 0.6–0.7 eV when going from an undoped CdSe particle to a Cu-doped CdSe particle. This is consistent with the Se environment effectively becoming "ionized" as the more electronegative Cu ion is substituted for a Cd site in the CdSe lattice. It was also found that there is an evidence for statistical ion doping, as opposed to ion clustering. The introduction of Cu^{+1} led to charge imbalances in the nanoparticle, which produced deep trap levels due to Se vacancies [37]. Doping of II-VI semiconductors is also discussed in Chaps. 4, 13, and 16.

QDs are sensitive to the optical radiation and can degrade under visible light in the oxygen-rich atmosphere. A photoetching technique is commonly used for controlled reduction of QD size. In order to understand a long-term photostability of colloidal CdSe QDs they were suspended in toluene and stored in combinations of light/dark and N_2/O_2 [38]. By subjecting the CdSe suspension to air and light oxidative transformations of the surface are accelerated. On the contrary, one can minimize surface oxidation through storage in a dark environment under an inert atmosphere. The protecting TOPO surface layer of QDs was decreased by washing in a toluene suspension with methanol. Figure 12.24 shows the Se K-edge XANES spectra for the QDs with reduced protective layer before and after light exposition.

XANES spectrum can be recorded by measuring X-ray fluorescence or UV-visible luminescence. Figure 12.25 shows the optically X-ray excited optical luminescence

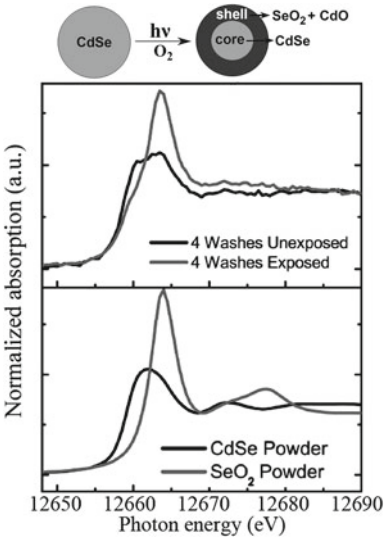

Fig. 12.24 Se K-edge XANES spectra for the CdSe colloidal nanoparticles after four washes. Comparison to spectra of CdSe and SeO_2 samples suggests that photoetched samples are partially oxidized. Adapted from [38]

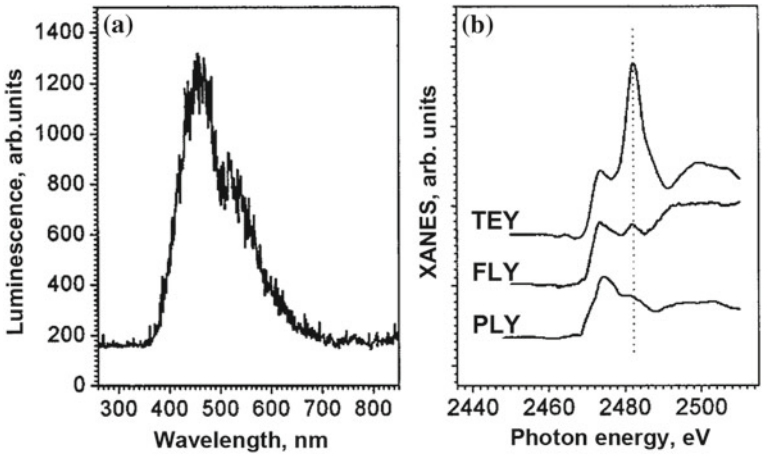

Fig. 12.25 **a** XEOL spectrum of CdS QDs excited at 2474 eV. **b** S K-edge XANES of CdS QDs measured in total electron yield (*TEY*), X-ray fluorescence yield (*FLY*) and total photoluminescence yield (*PLY*) modes. Adapted from [39]

(XEOL) spectrum of CdS QDs [39]. It displays a blue-light maximum emission at 465 nm followed by a shoulder at 520 nm. XEOL is very similar to the UV-excited spectrum because they involve similar recombination of holes in the valence band and electrons in the conduction band while only excitation process is different.

Authors have found that blue band in XEOL is very stable for more than 2 months in the atmosphere, indicating that each QD in the dendrimer aggregates does not degrade. When total UV-visible luminescence is counted as a function of an energy incident X-ray beam, a photoluminescence yield (PLY) XANES can be measured. Figure 12.25b shows the S K-edge XANES spectra recorded in bulk-sensitive X-ray fluorescence yield mode (TEY), surface sensitive total electron yield mode and PLY mode. Since only sulfur sites that produce photoluminescence efficiently will be responsible for the optical yield, the PLY spectrum provides information about the local structure of sulfur species contributing to the luminescence of the QDs.

A high resonance at 2482 eV in the TEY recorded XANES can be attributed to the absorption of sulfur in the form of sulfate SO_4^{2-} species it the nanometer-thick sulfate layer around QDs. Intensity of this resonance is reduced in the bulk sensitive FLY recorded XANES which reflects the CdS structure. Further reduction of the intensity of the SO_4^{2-} related resonance at 2482 eV is observed in PLY recorded XANES. And an important conclusion can be made that it is the S^{2-} species in CdS, but not SO_4^{2-} species that is responsible for the luminescence behavior of the QDs.

References

1. A.I. Ekimov, A.A. Onushchenko, JETP Lett. **34**, 345 (1981)
2. M.A. Reed, J.N. Randall, R.J. Aggarwal, R.J. Matyi, T.M. Moore, A.E. Wetsel, Phys. Rev. Lett. **60**, 535 (1988)
3. P. Harrison, *Quantum Wells, Wires and Dots: Theoretical and Computational Physics of Semiconductor Nanostructures* (Wiley, New York, 2005)
4. V.I. Klimov, *Nanocrystal Quantum Dots* (CRC Press Inc, 2010)
5. I.L. Medintz, H.T. Uyeda, E.R. Goldman, H. Mattoussi, Nat. Mater. **4**, 435 (2005)
6. Y. Zheng, S. Gao, J.Y. Ying, Adv. Mater. **19**, 376 (2007)
7. N. Fuke, L.B. Hoch, A.Y. Koposov, V.W. Manner, D.J. Werder, A. Fukui, N. Koide, H. Katayama, M. Sykora, ACS Nano. **4**, 6377 (2010)
8. K.S. Leschkies, A.G. Jacobs, D.J. Norris, E.S. Aydil, Appl. Phys. Lett. **95**, 193103 (2009)
9. M. Kroutvar, Y. Ducommun, D. Heiss, M. Bichler, D. Schuh, G. Abstreiter, J.J. Finley, Nature **432**, 81 (2004)
10. L. Goldstein, F. Glas, J.Y. Marzin, M.N. Charasse, G. Le Roux, Appl. Phys. Lett. **47**, 1099 (1985)
11. M.T. Björk, A. Fuhrer, A.E. Hansen, M.W. Larsson, L.E. Fröberg, L. Samuelson, Phys. Rev. B **72**, 201307 (2005)
12. N. Akopian, G. Patriarche, L. Liu, J.C. Harmand, V. Zwiller, Nano Letters **10**, 1198 (2010)
13. Y.J. Zeng, Z.Z. Ye, F. Liu, D.Y. Li, Y.F. Lu, W. Jaeger, H.P. He, L.P. Zhu, J.Y. Huang, B.H. Zhao, Cryst. Growth Des. **9**, 263 (2008)
14. X. Wang, J. Zhuang, Q. Peng, Y. Li, Nature **437**, 121 (2005)
15. J.B. Delehanty, K. Susumu, R.L. Manthe, W.R. Algar, I.L. Medintz, Anal. Chim. Acta **750**, 63 (2012)
16. W.R. Algar, K. Susumu, J.B. Delehanty, I.L. Medintz, Anal. Chem. **83**, 8826 (2011)
17. S. Horoz, L. Lu, Q. Dai, J. Chen, B. Yakami, J.M. Pikal, W. Wang, J. Tang, Appl. Phys. Lett. **101**, 223902 (2012)
18. S. Patra, B. Satpati, S.K. Pradhan, J. Appl. Phys. **106**, 034313 (2009)
19. P.M. Koenraad, M.E. Flatte, Nat. Mater. **10**, 91 (2011)
20. A. Jentys, Phys. Chem. Chem. Phys. **1**, 4059 (1999)

21. B. Gilbert, B.H. Frazer, H. Zhang, F. Huang, J.F. Banfield, D. Haskel, J.C. Lang, G. Srajer, G.D. Stasio, Phys. Rev. B **66**, 245205 (2002)
22. C. Brouder, J. Phys.: Condens. Matter **2**, 701 (1990)
23. J.H. Guo, L. Vayssieres, C. Persson, R. Ahuja, B. Johansson, J. Nordgren, J. Phys.: Condens. Matter **14**, 6969 (2002)
24. F. Decremps, F. Datchi, A.M. Saitta, A. Polian, S. Pascarelli, A. Di Cicco, J.P. Itié, F. Baudelet, Phys. Rev. B **68**, 104101 (2003)
25. S.B. Erenburg, N.V. Bausk, A.V. Dvurechenskii, Z.V. Smagina, A.V. Nenashev, A.I. Nikiforov, V.G. Mansurov, K.S. Zhuravlev, A.I. Toropov, J. Sur. Invest. X-ray, Synchrotron Neutron Tech. **1**, 26 (2007)
26. Y. Hori, X. Biquard, E. Monroy, D. Jalabert, F. Enjalbert, L.S. Dang, M. Tanaka, O. Oda, B. Daudin, Appl. Phys. Lett. **84**, 206 (2004)
27. F. d'Acapito, S. Colonna, F. Arciprete, A. Balzarotti, I. Davoli, F. Patella, S. Mobilio, Nucl. Instrum. Methods Phys. Res. Sect. B **200**, 85 (2003)
28. M. Ishii, K. Ozasa, Y. Aoyagi, Microelectron. Eng. **67–68**, 955 (2003)
29. D. Chen, C. Li, Z. Zhu, J. Fan, S. Wei, Phys. Rev. B **72** (2005)
30. M.S. Seehra, P. Dutta, S. Neeleshwar, Y.-Y. Chen, C.L. Chen, S.W. Chou, C.C. Chen, C.-L. Dong, C.-L. Chang, Adv. Mater. **20**, 1656 (2008)
31. E. Piskorska-Hommel, V. Holý, O. Caha, A. Wolska, A. Gust, C. Kruse, H. Kröncke, J. Falta, D. Hommel, J. Alloy Comp. **523**, 155 (2012)
32. H.M. Chen, C.K. Chen, C.C. Lin, R.-S. Liu, H. Yang, W.-S. Chang, K.-H. Chen, T.-S. Chan, J.-F. Lee, D.P. Tsai, J. Phys. Chem. C **115**, 21971 (2011)
33. W. Zheng, K. Singh, Z. Wang, J.T. Wright, J. van Tol, N.S. Dalal, R.W. Meulenberg, G.F. Strouse, J. Am. Chem. Soc. **134**, 5577 (2012)
34. E. Stavitski, F.M.F. de Groot, Micron **41**, 687 (2010)
35. Y. Qu, W. Li, Y. Zhou, X. Liu, L. Zhang, L. Wang, Y.-F. Li, A. Iida, Z. Tang, Y. Zhao, Z. Chai, C. Chen, Nano Letters **11**, 3174 (2011)
36. J.R.I. Lee, H.D. Whitley, R.W. Meulenberg, A. Wolcott, J.Z. Zhang, D. Prendergast, D.D. Lovingood, G.F. Strouse, T. Ogitsu, E. Schwegler, L.J. Terminello, T. van Buuren, Nano Letters **12**, 2763 (2012)
37. R.W. Meulenberg, T. van Buuren, K.M. Hanif, T.M. Willey, G.F. Strouse, L.J. Terminello, Nano Letters **4**, 2277 (2004)
38. D.A. Hines, M.A. Becker, P.V. Kamat, J. Phys. Chem. C **116**, 13452 (2012)
39. P. Zhang, S.J. Naftel, T.K. Sham, J. Appl. Phys. **90**, 2755 (2001)